Research Article

Numerical simulation of viscoelastic fluid–structure interaction benchmarks and their application to the human eye

Alexander Drobny[1] · Elfriede Friedmann[1]

Abstract

We present a numerical solution method for time-dependent viscoelastic fluid–structure interaction employing the arbitrary Lagrangian Eulerian framework. The derived monolithic variational formulation is discretized in time using the shifted Crank–Nicolson scheme and in space using the finite element method. For the linearisation we employ Newton's method with exact Jacobians. The viscoelastic fluid is modelled either using the Oldroyd-B or a Burgers-type model. The elastic structures are non-linear hyperelastic materials. We validate the implementation on benchmark problems and numerically analyse the convergence for global mesh refinement and adaptive mesh refinement using the dual-weighted residual method. Furthermore we numerically analyse the influence of the viscoelasticity of the fluid on typical goal functionals like the drag, the lift and the displacement. The derived numerical solution method is applied to ophthalmology where we analyse the interaction of the viscoelastic vitreous with its surrounding elastic structures.

Article highlights

- We obtain reliable results for the temporal and spatial discretization for a challenging viscoelastic FSI benchmark.
- We show good performance for the dual-weighted residual method for pure viscoelastic problems and for viscoelastic FSI.
- The viscoelasticity has a significant impact on the functionals of interest for the benchmarks and for the human eye.

1 Introduction

The research of fluid–structure interaction (FSI) problems is a continuously growing field. Many real world applications require the coupling of a fluid with an elastic solid. Typical examples can be found in hemodynamics [1, 2] and aerodynamics [3]. The application considered in this work is the human eye where the fluid-like vitreous interacts with its surrounding elastic structures like the sclera and the lens.

In many applications it is appropriate to use the incompressible Newtonian Navier–Stokes equations for the fluid model. In some cases this might not be sufficient for example if the fluid has non-Newtonian characteristics as in the case of blood vessels (see e.g. [4]) or viscoelastic properties as in the case of the vitreous [5, 6].

✉ Alexander Drobny, adrobny@mathematik.uni-kassel.de; Elfriede Friedmann, friedmann@mathematik.uni-kassel.de | [1]Institute of Mathematics, Kassel University, Heinrich-Plett-Straße 40, Kassel, Germany.

The goals of this contribution are the following: One objective is to numerically study viscoelastic FSI on benchmark problems from the literature which are commonly used for Newtonian FSI. This includes the stationary FSI1 and the instationary FSI3 benchmarks from [7]. To the best of our knowledge these viscoelastic FSI problems have not been studied before. We study the convergence of functionals like the drag, the lift and the displacement at a specific point and analyse the effect of the viscoelasticity on these functionals. Furthermore we apply the dual-weighted residual (DWR) method to viscoelastic fluids and viscoelastic FSI. To the best of our knowledge the DWR method has not been analysed for these problems before. We numerically analyse the convergence under global mesh refinement and adaptive mesh refinement using the DWR method. Finally we apply the numerical methods to ophthalmology where we perform simulations in a realistic human eye geometry similar to recent experiments in [8]. This seems necessary since experiments have shown that the vitreous has significant viscoelastic properties [5, 6].

One of the main difficulties in the modelling and the finite element simulation of FSI is the coupling of the fluid and the solid. While the fluid equations are usually formulated in the Eulerian framework, structure equations commonly use the Lagrangian framework. We cope with this by employing the arbitrary Lagrangian Eulerian (ALE) method [9].

To this end we derive a monolithic variational formulation of the viscoelastic FSI equations. The viscoelastic fluid is modelled as a Burgers-type or Oldroyd-B fluid. The elastic structure is modelled as a hyperelastic material. The variational formulation is discretized in time using the shifted Crank–Nicolson scheme. Spatial discretization is done using the finite element method. Since the equations are non-linear we use Newton's method with exact Jacobians for the linearisation. The resulting linear system is solved using the parallel direct solver Mumps [10].

The ALE method has been studied numerically in the literature for FSI with Newtonian fluids (see e.g. [11, 12]). Alternative approaches are for example partitioned methods (see e.g. [13, 14]) and Eulerian methods (see e.g. [15]). Partitioned methods are mostly used for weakly coupled problems. Eulerian methods have the advantage of being able to handle large deformations and topology changes. While topology changes are not possible with the ALE approach, large deformations are possible as long as there is no mesh degeneration.

Viscoelastic fluids have been studied numerically in the literature as well (see e.g. [16, 17]). Our focus is on a viscoelastic Burgers-type model which was studied for example in [18] for fluid problems in the ALE framework. This model has been shown to be capable of modelling the viscoelastic behaviour of the vitreous [5, 6]. Furthermore we consider the more common Oldroyd-B model which can be seen as a special case of the Burgers-type equations.

The DWR method [19] allows local mesh refinement with the aim of increasing the accuracy in certain goal functionals like the drag or the lift. The DWR method has been applied to Newtonian fluid and Newtonian FSI problems in ALE coordinates in the literature (see e.g. [15, 20–22]). In this work the performance of the DWR method is studied for viscoelastic fluids and viscoelastic FSI.

Results on FSI in the human eye are sparse. In [23] a FSI problem in the eye consisting of the anterior chamber and the iris, using the Navier–Stokes equations and a simple elasticity law, was studied. In [24] simulations in bovine eyes were analysed where the interaction of the viscoelastic vitreous with the sclera and lens was studied. Due to the high computational costs low-order finite elements were used. In Section 5.4 we study a similar experiment on a human eye geometry using higher order finite elements.

2 Modelling

In this section we state the fluid and the solid equations in their usual frameworks and combine the equations to the coupled FSI problem before deriving the monolithic variational formulation in the next section.

In the following we denote the, possibly time-dependent fluid domain by $\Omega_f \subset \mathbb{R}^d$, $d = 2, 3$ and its boundary by $\partial\Omega_f$. The current solid domain is denoted by $\Omega_s \subset \mathbb{R}^d$ and its boundary by $\partial\Omega_s$. The whole domain is denoted by $\Omega := \overline{\Omega_f \cup \Omega_s} \setminus (\partial\Omega_f \cup \partial\Omega_s)$ with the common interface $\Gamma_i := \partial\Omega_f \cap \partial\Omega_s$. The corresponding reference domains are denoted by $\hat{\Omega}$, $\hat{\Omega}_f$ and $\hat{\Omega}_s$, respectively. The time interval is given by $I = (0, T], T > 0$.

We define the deformation of the structure domain $\hat{\Omega}_s$ as the following mapping

$$\hat{T}_s : I \times \hat{\Omega}_s \to \Omega_s \quad \text{with } x = \hat{T}_s(t, \hat{x})$$

and the deformation gradient $\hat{F} : \hat{\Omega}_s \to \mathbb{R}^{d \times d}$ by

$$\hat{F} := \hat{F}(\hat{u}_s) := \hat{\nabla}\hat{T}_s = \hat{I} + \hat{\nabla}\hat{u}_s$$

with the identity matrix $\hat{I}$ and the displacement $\hat{u}_s$.

The ALE formulation is based on an artificial displacement $\hat{u}_f(t, \hat{x})$ in the fluid domain and on the ALE mapping

$$\hat{T}_f \, : \, I \times \hat{\Omega}_f \to \Omega_f, \quad \hat{T}_f(t,\hat{x}) = \hat{x} + \hat{u}_f(t,\hat{x}).$$

The deformation gradient is defined as

$$\hat{F} := \hat{F}(\hat{u}_f) := \hat{\nabla} \hat{T}_f = \hat{I} + \hat{\nabla} \hat{u}_f.$$

In the following we assume that $\hat{T}_s$ and $\hat{T}_f$ are C^1-diffeomorphisms.

2.1 Fluid equations

Motivated by experiments on human eyes in [6] we model the fluid using a viscoelastic Burgers model [25] with additional Newtonian dissipation. The corresponding one-dimensional analogon is depicted in Fig. 1 and consists of the parallel connection of a dashpot and two serial connections of a spring and a dashpot. This one-dimensional analogon can be generalized to two and three dimensions (see e.g. [17]). Following [18] this Burgers-type model can be written in the following form

$$\rho_f \partial_t v_f + \rho_f (v_f \cdot \nabla) v_f - \mathrm{div}\,\mathbb{T}_f = \rho_f f_f \quad \text{in } \Omega_f, t \in I$$
$$\mathrm{div}\, v_f = 0 \quad \text{in } \Omega_f, t \in I$$
$$\overset{\triangledown}{B_1} + \frac{\mu_1}{\nu_1}(B_1 - I) = 0 \quad \text{in } \Omega_f, t \in I$$
$$\overset{\triangledown}{B_2} + \frac{\mu_2}{\nu_2}(B_2 - I) = 0 \quad \text{in } \Omega_f, t \in I$$

with the Cauchy stress tensor

$$\mathbb{T}_f = -p_f I + \rho_f \nu_f (\nabla v_f + \nabla v_f^T) + \mu_1(B_1 - I) + \mu_2(B_2 - I) \quad (1)$$
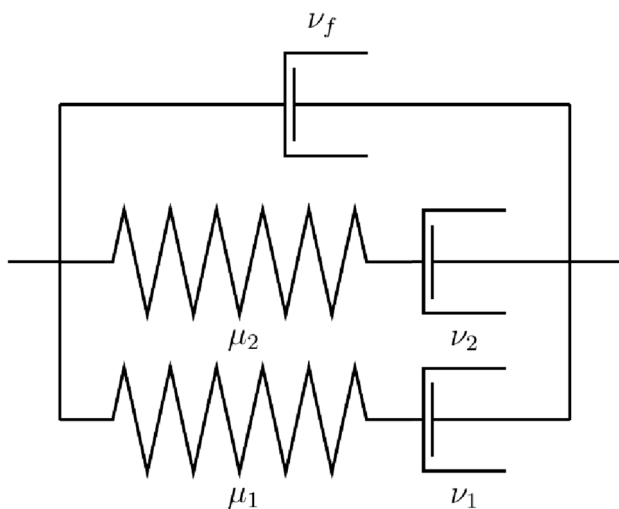
and the upper convected Oldroyd derivative

Fig. 1 The Burgers-type element

$$\overset{\triangledown}{S} := \partial_t S + (v_f) \cdot \nabla) S - (\nabla v_f) S - S(\nabla v_f))^T.$$

Here v_f is the velocity of the fluid, ρ_f the density, ν_f the viscosity, p_f the pressure, f_f a possible force term, B_1 and B_2 are tensor-valued unknowns and μ_1, μ_2, ν_1, ν_2 are parameters characterizing the viscoelasticity of the fluid.

For $\mu_0 := \mu_1 + \mu_2$ and $\nu_0 := \nu_1 = \nu_2$ and using the same boundary and initial conditions for B_1 and B_2 in the Burgers model we obtain the Oldroyd-B model

$$\rho_f \partial_t v_f + \rho_f (v_f \cdot \nabla) v_f - \mathrm{div}\,\mathbb{T}_f = \rho_f f_f \quad \text{in } \Omega_f, t \in I$$
$$\mathrm{div}\, v_f = 0 \quad \text{in } \Omega_f, t \in I$$
$$\overset{\triangledown}{B} + \frac{\mu_0}{\nu_0}(B - I) = 0 \quad \text{in } \Omega_f, t \in I$$

with the Cauchy stress tensor

$$\mathbb{T}_f = -p_f I + \rho_f \nu_f (\nabla v_f + \nabla v_f^T) + \mu_0(B - I)$$

and with $B = B_1 + B_2$.

Furthermore we consider the incompressible Newtonian Navier–Stokes equations which are obtained by dropping the terms involving the viscoelastic tensors B_1 and B_2:

$$\rho_f \partial_t v_f + \rho_f (v_f \cdot \nabla) v_f - \mathrm{div}\,\mathbb{T}_f = \rho_f f_f \quad \text{in } \Omega_f, t \in I$$
$$\mathrm{div}\, v_f = 0 \quad \text{in } \Omega_f, t \in I$$

with the Cauchy stress tensor

$$\mathbb{T}_f = -p_f I + \rho_f \nu_f (\nabla v_f + \nabla v_f^T).$$

2.2 Solid equations

The elastic structure is modelled as a hyperelastic non-linear material. Let $\hat{u}_s$ be the displacement, $\hat{\rho}_s$ the density and $\hat{f}_s$ a force term. Conservation of momentum in the Lagrangian framework reads

$$\hat{\rho}_s \partial_t^2 \hat{u}_s - \widehat{\mathrm{div}}(\hat{\Pi}) = \hat{\rho}_s \hat{f}_s \quad \text{in } \hat{\Omega}_s, t \in I$$

with the first Piola–Kirchhoff stress tensor $\hat{\Pi}$. For the benchmark simulations we use the Saint–Venant–Kirchhoff (STVK) material where the first Piola–Kirchhoff stress tensor is given by

$$\hat{\Pi} := \hat{F}(2\mu \hat{E} + \lambda \mathrm{tr}(\hat{E})\hat{I}) \quad (2)$$

with $\hat{E} := \frac{1}{2}(\hat{F}^T \hat{F} - \hat{I})$ and $\hat{F} := \hat{I} + \hat{\nabla} \hat{u}_s$. Here λ and μ are the first and second Lamé constants. For the application to the human eye in Sect. 5.4 we use an isochoric Neo-Hookean material with the strain-energy function [26, 27]:

$$\hat{W} = \frac{1}{2}\mu\left(\hat{J}^{-2/3}\mathrm{tr}\hat{C} - 3\right) + \frac{1}{2}\kappa \, (\ln \hat{J})^2$$

with the right Cauchy–Green tensor $\hat{C} = \hat{F}^T\hat{F}$ and $\hat{J} = \det\hat{F}$. For the Piola–Kirchhoff stress tensor we obtain

$$\hat{\Pi} = \frac{\partial \hat{W}}{\partial \hat{F}} = \mu\hat{J}^{-2/3}\left(\hat{F} - \frac{1}{3}\text{tr}(\hat{C})\hat{F}^{-T}\right) \tag{3}$$
$$+ \kappa\ln\hat{J}\hat{F}^{-T}.$$

2.3 FSI equations

We combine the fluid and the solid equations to the coupled FSI problem. For the structure equations we use a mixed formulation where we define the velocity $\hat{v}_s = \partial_t\hat{u}_s$. Then the coupled viscoelastic FSI problem reads:

$$\rho_f\partial_t v_f + \rho_f(v_f\cdot\nabla)v_f - \text{div}\mathbb{T}_f = \rho_f f_f \quad \text{in } \Omega_f, t\in I$$

$$\text{div} v_f = 0 \quad \text{in } \Omega_f, t\in I$$

$$\partial_t B_1 + (v_f\cdot\nabla)B_1 - (\nabla v_f)B_1 - B_1(\nabla v_f)^T + \frac{\mu_1}{\nu_1}(B_1 - I) = 0 \quad \text{in } \Omega_f, t\in I$$

$$\partial_t B_2 + (v_f\cdot\nabla)B_2 - (\nabla v_f)B_2 - B_2(\nabla v_f)^T + \frac{\mu_2}{\nu_2}(B_2 - I) = 0 \quad \text{in } \Omega_f, t\in I$$

$$\hat{\rho}_s\partial_t\hat{v}_s - \widehat{\text{div}}(\hat{\Pi}) = \hat{\rho}_s\hat{f}_s \quad \text{in } \hat{\Omega}_s, t\in I$$

$$\partial_t\hat{u}_s - \hat{v}_s = 0 \quad \text{in } \hat{\Omega}_s, t\in I$$

with the stress tensors defined as in Eqs. (1) and (2) or (3) depending on the chosen material. This strong form has to be supplemented with appropriate initial, boundary and interface conditions. Here the fluid equations are formulated on moving domains in Eulerian coordinates, while the structure equations are formulated in the Lagrangian framework. We cope with this by deriving a monolithic variational formulation on fixed domains in the ALE framework.

3 Variational formulation and discretization

In the following we state the monolithic variational formulation for viscoelastic FSI. Then we summarize the necessary steps for the numerical discretization. This includes the temporal discretization, spatial discretization and the linearisation using Newton's method.

3.1 Variational formulation

The ALE transformation in the fluid domain is defined using a standard harmonic extension with a diffusion parameter $\alpha_u \in \mathbb{R}_+$. The interface conditions are continuity of the velocities, displacements and normal stresses. The continuity of the normal stresses is fulfilled in a weak sense. The boundary of the fluid domain $\hat{\Omega}_f$ is split into three parts: the Dirichlet boundary, the Neumann boundary and the interface: $\partial\hat{\Omega}_f = \hat{\Gamma}_{f,D} \cup \hat{\Gamma}_{f,N} \cup \hat{\Gamma}_i$. Analogously we split the boundary of the structure domain

$\partial\hat{\Omega}_s = \hat{\Gamma}_{s,D} \cup \hat{\Gamma}_{s,N} \cup \hat{\Gamma}_i$. Next we define the following function spaces

$$\hat{W}_f := H^1(\hat{\Omega}_f)^{d\times d},$$
$$H_0^1(\hat{\Omega}_f)^d := \{\hat{v}_f \in H^1(\hat{\Omega}_f)^d : \hat{v}_f = 0 \text{ on } \hat{\Gamma}_{f,D}\},$$
$$H_0^1(\hat{\Omega}_s)^d := \{\hat{v}_s \in H^1(\hat{\Omega}_s)^d : \hat{v}_s = 0 \text{ on } \hat{\Gamma}_{s,D}\},$$
$$\hat{V}_{f,\hat{v}}^{d,0} := \{\hat{v}_f \in H_0^1(\hat{\Omega}_f)^d : \hat{v}_f = \hat{v}_s \text{ on } \hat{\Gamma}_i\},$$
$$\hat{V}_{f,\hat{u}}^{d,0} := \{\hat{u}_f \in H_0^1(\hat{\Omega}_f)^d : \hat{u}_f = \hat{u}_s \text{ on } \hat{\Gamma}_i\},$$
$$\hat{V}_{f,\hat{\Gamma}_i}^{d,0} := \{\hat{\psi}_f \in H_0^1(\hat{\Omega}_f)^d : \hat{\psi}_f = \hat{\psi}_s \text{ on } \hat{\Gamma}_i\},$$
$$\hat{V}_{f,\hat{u},\hat{\Gamma}_i}^{d,0} := \{\hat{\psi}_f \in H_0^1(\hat{\Omega}_f)^d : \hat{\psi}_f = 0 \text{ on } \hat{\Gamma}_i\}.$$

Then the variational formulation transformed to the reference domain reads:

Problem 1 Find $\{\hat{v}_f, \hat{v}_s, \hat{u}_f, \hat{u}_s, \hat{p}_f, \hat{B}_1, \hat{B}_2\} \in \{\hat{v}_f^D + \hat{V}_{f,\hat{v}}^{d,0}\}$ $\times\{\hat{v}_s^D + H_0^1(\hat{\Omega}_s)^d\} \times \{\hat{u}_f^D + \hat{V}_{f,\hat{u}}^{d,0}\} \times \{\hat{u}_s^D + H_0^1(\hat{\Omega}_s)^d\} \times L^2(\hat{\Omega}_f)$ $\times\hat{W}_f \times \hat{W}_f$ such that the initial conditions $\hat{v}_f(0) = \hat{v}_f^0$, $\hat{v}_s(0) = \hat{v}_s^0, \hat{u}_f(0) = \hat{u}_f^0, \hat{u}_s(0) = \hat{u}_s^0, \hat{B}_1(0) = \hat{I}, \hat{B}_2(0) = \hat{I}$ are fulfilled and for almost all time steps $t \in I$ it holds:

$$(\hat{J}\hat{\rho}_f\partial_t\hat{v}_f, \hat{\psi}_f^v)_{\hat{\Omega}_f} + (\rho_f\hat{J}(\hat{F}^{-1}(\hat{v}_f - \partial_t\hat{u}_f)\cdot\hat{\nabla})\hat{v}_f, \hat{\psi}_f^v)_{\hat{\Omega}_f}$$
$$+ (\hat{J}\hat{\mathbb{T}}_f\hat{F}^{-T}, \hat{\nabla}\hat{\psi}_f^v)_{\hat{\Omega}_f} - \langle\hat{J}\hat{\mathbb{T}}_f\hat{F}^{-T}\hat{n}_f, \hat{\psi}_f^v\rangle_{\hat{\Gamma}_{f,N}} - (\hat{\rho}_f\hat{J}\hat{f}_f, \hat{\psi}_f^v)_{\hat{\Omega}_f}$$
$$= 0, \left(\hat{J}\left(\partial_t\hat{B}_1 + (\hat{\nabla}\hat{B}_1)(\hat{F}^{-1}(\hat{v}_f - \partial_t\hat{u}_f))\right)\right.$$
$$\left. - (\hat{\nabla}\hat{v}_f)\hat{F}^{-1}\hat{B}_1 - \hat{B}_1\hat{F}^{-T}(\hat{\nabla}\hat{v}_f)^T + \frac{\mu_1}{\nu_1}(\hat{B}_1 - \hat{I})\right), \hat{\psi}^{B_1}\right)_{\hat{\Omega}_f}$$
$$= 0, \left(\hat{J}\left(\partial_t\hat{B}_2 + (\hat{\nabla}\hat{B}_2)(\hat{F}^{-1}(\hat{v}_f - \partial_t\hat{u}_f))\right)\right.$$
$$\left. - (\hat{\nabla}\hat{v}_f)\hat{F}^{-1}\hat{B}_2 - \hat{B}_2\hat{F}^{-T}(\hat{\nabla}\hat{v}_f)^T + \frac{\mu_2}{\nu_2}(\hat{B}_2 - \hat{I})\right), \hat{\psi}^{B_2}\right)_{\hat{\Omega}_f}$$
$$= 0, (\hat{\rho}_s\partial_t\hat{v}_s, \hat{\psi}_s^v)_{\hat{\Omega}_s} + (\hat{\Pi}, \hat{\nabla}\hat{\psi}_s^v)_{\hat{\Omega}_s} - \langle\hat{\Pi}\hat{n}_s, \hat{\psi}_s^v\rangle_{\hat{\Gamma}_{s,N}} - (\hat{\rho}\hat{f}_s, \hat{\psi}_s^v)_{\hat{\Omega}_s}$$
$$= 0, (\partial_t\hat{u}_s - \hat{v}_s, \hat{\psi}_s^u)_{\hat{\Omega}_s} = 0, \left(\widehat{\text{div}}(\hat{J}\hat{F}^{-1}\hat{v}_f), \hat{\psi}_f^p\right)_{\hat{\Omega}_f}$$
$$= 0, (\alpha_u\hat{\nabla}\hat{u}_f, \hat{\nabla}\hat{\psi}_f^u)_{\hat{\Omega}_f} = 0\forall\hat{\psi}_f^v \in \hat{V}_{f,\hat{\Gamma}_i}^{d,0}, \forall\hat{\psi}^{B_1} \in \hat{W}_f,$$
$$\forall\hat{\psi}^{B_2} \in \hat{W}_f, \forall\hat{\psi}_s^v \in H_0^1(\hat{\Omega}_s)^d, \forall\hat{\psi}_s^u \in L^2(\hat{\Omega}_s)^d, \forall\hat{\psi}_f^p \in L^2(\hat{\Omega}_f), \forall\hat{\psi}_f^u \in \hat{V}_{f,\hat{u},\hat{\Gamma}_i}^{d,0}$$

with

$$\hat{\mathbb{T}}_f = -\hat{p}_f\hat{I} + \hat{\rho}_f\nu_f\left(\hat{\nabla}\hat{v}_f\hat{F}^{-1} + \hat{F}^{-T}\hat{\nabla}\hat{v}_f^T\right)$$
$$+ \mu_1(\hat{B}_1 - \hat{I}) + \mu_2(\hat{B}_2 - \hat{I}).$$

Additionally we assume that $\hat{T}_s$ and $\hat{T}_f$ are C^1-diffeomorphisms.

Here $(\cdot,\cdot)_{\hat{\Omega}_f}$ denotes the usual $L^2(\hat{\Omega}_f)$ product. One possible choice for the Neumann boundary condition is the do-nothing condition

$$\hat{\rho}_f v_f \hat{\nabla}\hat{v}_f \hat{F}^{-1}\hat{n}_f - \hat{p}_f \hat{n}_f = 0 \text{ on } \hat{\Gamma}_{f,N}$$

which yields the following correction term in the variational formulation [28]

$$\left\langle \hat{J}\hat{\mathbb{T}}_f \hat{F}^{-T}\hat{n}_f, \hat{\psi}_f^v \right\rangle_{\hat{\Gamma}_{f,N}} = \left\langle \hat{J}\left(\hat{\rho}_f v_f \hat{F}^{-T}\hat{\nabla}\hat{v}_f^T + \mu_1(\hat{B}_1 - \hat{I})\right.\right.$$
$$\left.\left. + \mu_2(\hat{B}_2 - \hat{I})\right)\hat{F}^{-T}\hat{n}_f, \hat{\psi}_f^v \right\rangle_{\hat{\Gamma}_{f,N}}.$$

For a detailed derivation of the variational formulation of Newtonian FSI and its discretization we refer to [29, 30].

3.2 Temporal discretization

For the temporal discretization we use one-step-θ schemes. Depending on the choice of θ we obtain the backward Euler ($\theta = 1.0$), the Crank–Nicolson ($\theta = 0.5$) or the shifted Crank–Nicolson scheme ($\theta = 0.5 + \mathcal{O}(\Delta t)$) where Δt is the time step size [31]. To this end we define the semilinear form $\hat{A}(\cdot, \cdot)$ corresponding to Problem 1 as:

$$\hat{A}(\hat{U}, \hat{\psi}) = \left(\hat{J}\hat{\rho}_f \partial_t \hat{v}_f, \hat{\psi}_f^v\right)_{\hat{\Omega}_f} + \left(\hat{\rho}_f \hat{J}(\hat{F}^{-1}(\hat{v}_f - \partial_t \hat{u}_f)\cdot \hat{\nabla})\hat{v}_f, \hat{\psi}_f^v\right)_{\hat{\Omega}_f}$$
$$+ \left(\hat{J}\hat{\mathbb{T}}_f \hat{F}^{-T}, \hat{\nabla}\hat{\psi}_f^v\right)_{\hat{\Omega}_f} - \left\langle \hat{J}\hat{\mathbb{T}}_f \hat{F}^{-T}\hat{n}_f, \hat{\psi}_f^v\right\rangle_{\hat{\Gamma}_{f,N}} - \left(\hat{\rho}_f \hat{J}\hat{f}_f, \hat{\psi}_f^v\right)_{\hat{\Omega}_f}$$
$$+ \left(\hat{J}\left(\partial_t \hat{B}_1 + (\hat{\nabla}\hat{B}_1)(\hat{F}^{-1}(\hat{v}_f - \partial_t \hat{u}_f)) - (\hat{\nabla}\hat{v}_f)\hat{F}^{-1}\hat{B}_1 - \hat{B}_1 \hat{F}^{-T}(\hat{\nabla}\hat{v}_f)^T \right.\right.$$
$$\left.\left. + \frac{\mu_1}{\nu_1}(\hat{B}_1 - \hat{I})\right), \hat{\psi}^{B_1}\right)_{\hat{\Omega}_f} + \left(\hat{J}\left(\partial_t \hat{B}_2 + (\hat{\nabla}\hat{B}_2)(\hat{F}^{-1}(\hat{v}_f - \partial_t \hat{u}_f))\right.\right.$$
$$\left.\left. - (\hat{\nabla}\hat{v}_f)\hat{F}^{-1}\hat{B}_2 - \hat{B}_2 \hat{F}^{-T}(\hat{\nabla}\hat{v}_f)^T + \frac{\mu_2}{\nu_2}(\hat{B}_2 - \hat{I})\right), \hat{\psi}^{B_2}\right)_{\hat{\Omega}_f}$$
$$+ \left(\hat{\rho}_s \partial_t \hat{v}_s, \hat{\psi}_s^v\right)_{\hat{\Omega}_s} + \left(\hat{\Pi}, \hat{\nabla}\hat{\psi}_s^v\right)_{\hat{\Omega}_s} - \left\langle \hat{\Pi}\hat{n}_s, \hat{\psi}_s^v\right\rangle_{\hat{\Gamma}_{s,N}} - \left(\hat{\rho}\hat{f}_s, \hat{\psi}_s^v\right)_{\hat{\Omega}_s}$$
$$+ \left(\partial_t \hat{u}_s - \hat{v}_s, \hat{\psi}_s^u\right)_{\hat{\Omega}_s} + \left(\widehat{\mathrm{div}}(\hat{J}\hat{F}^{-1}\hat{v}_f), \hat{\psi}_f^p\right)_{\hat{\Omega}_f} + \left(\alpha_u \hat{\nabla}\hat{u}_f, \hat{\nabla}\hat{\psi}_f^u\right)_{\hat{\Omega}_f}.$$

Next we split $\hat{A}(\cdot, \cdot)$ into terms involving the time derivatives $(\hat{A}_T(\cdot)(\cdot))$, terms which are treated implicitly $(\hat{A}_I(\cdot)(\cdot))$ and the remaining terms $(\hat{A}_R(\cdot)(\cdot))$. The terms which are treated implicitly are the pressure term, the incompressibility condition and the mesh motion equation. For the terms involving the temporal derivatives

$$\hat{A}_T(\hat{U})(\hat{\psi}) = \left(\hat{J}\hat{\rho}_f \partial_t \hat{v}_f, \hat{\psi}_f^v\right)_{\hat{\Omega}_f} - \left(\hat{\rho}_f \hat{J}(\hat{F}^{-1}\partial_t \hat{u}_f \cdot \hat{\nabla})\hat{v}_f, \hat{\psi}_f^v\right)_{\hat{\Omega}_f}$$
$$+ \left(\hat{\rho}_s \partial_t \hat{v}_s, \hat{\psi}_s^v\right)_{\hat{\Omega}_s} + \left(\partial_t \hat{u}_s, \hat{\psi}_s^u\right)_{\hat{\Omega}_s},$$
$$+ \sum_{i=1}^{2}\left(\left(\hat{J}\partial_t \hat{B}_i, \hat{\psi}^{B_i}\right)_{\hat{\Omega}_f} - \left(\hat{J}\hat{\nabla}\hat{B}_i(\hat{F}^{-1}\partial_t \hat{u}_f), \hat{\psi}^{B_i}\right)_{\hat{\Omega}_f}\right)$$

this yields

$$\hat{A}_T(\hat{U}^{n,\Delta t})(\hat{\psi})$$
$$\approx \frac{1}{\Delta t}\hat{\rho}_f \left((\theta \hat{J}^n + (1-\theta)\hat{J}^{n-1})(\hat{v}_f^n - \hat{v}_f^{n-1}), \hat{\psi}_f^v\right)_{\hat{\Omega}_f}$$
$$- \frac{\theta}{\Delta t}\left(\hat{\rho}_f(\hat{J}^n \hat{F}^{-1}(t_n)(\hat{u}_f^n - \hat{u}_f^{n-1})\cdot \hat{\nabla})\hat{v}_f^n, \hat{\psi}_f^v\right)_{\hat{\Omega}_f}$$
$$- \frac{1-\theta}{\Delta t}\left(\hat{\rho}_f(\hat{J}^{n-1}\hat{F}^{-1}(t_{n-1})(\hat{u}_f^n - \hat{u}_f^{n-1})\cdot \hat{\nabla})\hat{v}_f^{n-1}, \hat{\psi}_f^v\right)_{\hat{\Omega}_f}$$
$$+ \frac{1}{\Delta t}\hat{\rho}_s \left(\hat{v}_s^n - \hat{v}_s^{n-1}, \hat{\psi}_s^v\right)_{\hat{\Omega}_s} + \frac{1}{\Delta t}\left(\hat{u}_s^n - \hat{u}_s^{n-1}, \hat{\psi}_s^u\right)_{\hat{\Omega}_s}$$
$$+ \frac{1}{\Delta t}\sum_{i=1}^{2}\left(\left((\theta \hat{J}^n + (1-\theta)\hat{J}^{n-1})(\hat{B}_i^n - \hat{B}_i^{n-1}), \hat{\psi}^{B_i}\right)_{\hat{\Omega}_f}\right.$$
$$- \theta\left(\hat{J}^n \hat{\nabla}\hat{B}_i^n(\hat{F}^{-1}(t_n)(\hat{u}_f^n - \hat{u}_f^{n-1})), \hat{\psi}^{B_i}\right)_{\hat{\Omega}_f}$$
$$\left. - (1-\theta)\left(\hat{J}^{n-1}\hat{\nabla}\hat{B}_i^{n-1}(\hat{F}^{-1}(t_{n-1})(\hat{u}_f^n - \hat{u}_f^{n-1})), \hat{\psi}^{B_i}\right)_{\hat{\Omega}_f}\right).$$

Here we abbreviated the variables in the current time step n and the previous time step $n-1$ using the superscript n and $n-1$, respectively.

With this the one-step-θ scheme reads: For a given previous time step solution $\hat{U}^{n-1} = \left\{\hat{v}_f^{n-1}, \hat{v}_s^{n-1}, \hat{u}_f^{n-1}, \hat{u}_s^{n-1}, \hat{p}_f^{n-1}, \hat{B}_1^{n-1}, \hat{B}_2^{n-1}\right\}$ find $\hat{U}^n = \left\{\hat{v}_f^n, \hat{v}_s^n, \hat{u}_f^n, \hat{u}_s^n, \hat{p}_f^n, \hat{B}_1^n, \hat{B}_2^n\right\}$ such that

$$\hat{A}_T(\hat{U}^{n,\Delta t})(\hat{\psi}) + \hat{A}_I(\hat{U}^n)(\hat{\psi}) + \theta \hat{A}_R(\hat{U}^n)(\hat{\psi})$$
$$= -(1-\theta)\hat{A}_R(\hat{U}^{n-1})(\hat{\psi}).$$

3.3 Spatial discretization

The spatial discretization is done using the finite element method. For the finite elements we choose biquadratic/triquadratic continuous elements for the velocity, displacement and for the viscoelastic tensors and linear discontinuous elements for the pressure, resulting in the finite element combination $Q_2^d \times Q_2^d \times P_1^{\mathrm{disc}} \times Q_2^{d\times d} \times Q_2^{d\times d}$ for velocity, displacement, pressure and the two viscoelastic tensors. The combination of velocity and pressure space satisfies the inf-sup condition (see e.g. [30]).

3.4 Linearisation

The non-linear system which is obtained after temporal and spatial discretization is solved using Newton's method. To this end we have to solve linear equations of the following form for $\delta \hat{U}^n$ in every time step:

$$\hat{A}'(\hat{U}^n)(\delta\hat{U}^n, \hat{\psi}) = \hat{F}(\hat{\psi}) - \hat{A}(\hat{U}^n)(\hat{\psi}) \quad \forall \hat{\psi} \in \hat{V}.$$

Here n denotes the time step. The semilinear form $\hat{A}(\hat{U}^n)(\hat{\psi})$ and right hand side $\hat{F}(\hat{\psi})$ correspond to terms in the variational formulation given in Problem 1. The Gateaux derivative of $\hat{A}(\hat{U}^n)(\hat{\psi})$ in direction $\delta\hat{U} := (\delta\hat{v}, \delta\hat{u}, \delta\hat{p}, \delta\hat{B}_1, \delta\hat{B}_2)$ is denoted by $\hat{A}'(\hat{U}^n)(\delta\hat{U}^n, \hat{\psi})$. For the sake of overview we only derive the linearisation for the terms related to the viscoelastic tensors and the Neo-Hookean elastic material. For details on the Gateaux derivative we refer to [32]. For a detailed derivation of the Gateaux derivative for Newtonian FSI with the STVK material we refer to [29] and [30]. We assume that the temporal discretization is done using the backward Euler scheme. Other time discretization methods like the shifted Crank–Nicolson scheme can be treated analogously.

We start with the terms including the time derivatives and then consider the remaining terms.

Proposition 2 *After temporal discretization of*

$$\hat{A}_T^{\text{visco}}(\hat{U})(\hat{\psi})$$

$$= \sum_{i=1}^{2} \left((\hat{J}\partial_t\hat{B}_i, \hat{\psi}^{B_i})_{\hat{\Omega}_f} - (\hat{J}\hat{\nabla}\hat{B}_i(\hat{F}^{-1}\partial_t\hat{u}_f), \hat{\psi}^{B_i})_{\hat{\Omega}_f} \right)$$

using the backward Euler scheme with time step size Δt we obtain

$$\hat{A}_T^{\text{visco}\prime}(\hat{U})(\delta\hat{U}, \hat{\psi}) = \sum_{i=1}^{2} \left(\left(\frac{1}{\Delta t}\hat{J}\delta\hat{B}_i, \hat{\psi}^{B_i} \right)_{\hat{\Omega}_f} \right.$$

$$+ \left(\frac{1}{\Delta t}\hat{J}\text{tr}(\hat{F}^{-1}\hat{\nabla}\delta\hat{u}_f)(\hat{B}_i - \hat{B}_i^{n-1}), \hat{\psi}^{B_i} \right)_{\hat{\Omega}_f}$$

$$- \left(\frac{1}{\Delta t}\hat{J}\text{tr}(\hat{F}^{-1}\hat{\nabla}\delta\hat{u}_f)\hat{\nabla}\hat{B}_i(\hat{F}^{-1}(\hat{u}_f - \hat{u}_f^{n-1})), \hat{\psi}^{B_i} \right)_{\hat{\Omega}_f}$$

$$- \left(\frac{1}{\Delta t}\hat{J}\hat{\nabla}\delta\hat{B}_i(\hat{F}^{-1}(\hat{u}_f - \hat{u}_f^{n-1})), \hat{\psi}^{B_i} \right)_{\hat{\Omega}_f}$$

$$- \left(\frac{1}{\Delta t}\hat{J}\hat{\nabla}\hat{B}_i((-\hat{F}^{-1}\hat{\nabla}\delta\hat{u}_f\hat{F}^{-1})(\hat{u}_f - \hat{u}_f^{n-1})), \hat{\psi}^{B_i} \right)_{\hat{\Omega}_f}$$

$$\left. - \left(\frac{1}{\Delta t}\hat{J}\hat{\nabla}\hat{B}_i(\hat{F}^{-1}\delta\hat{u}_f), \hat{\psi}^{B_i} \right)_{\hat{\Omega}_f} \right).$$

Proof Since the domain of integration is fixed and independent of the solution, the order of integration and differentiation can be switched. The result is then obtained from calculations based on well-known properties of the Gateaux derivative, see e.g. [32]. □

Proposition 3 *For the directional derivative of*

$$\hat{A}_R^{\text{visco}}(\hat{U})(\hat{\psi})$$

$$= \sum_{i=1}^{2} \left(\left(\hat{J}\hat{\nabla}\hat{B}_i(\hat{F}^{-1}\hat{v}_f), \hat{\psi}^{B_i} \right)_{\hat{\Omega}_f} - \left(\hat{J}\hat{\nabla}\hat{v}_f\hat{F}^{-1}\hat{B}_i, \hat{\psi}^{B_i} \right)_{\hat{\Omega}_f} \right.$$

$$\left. - \left(\hat{J}\hat{B}_i\hat{F}^{-T}\hat{\nabla}\hat{v}_f^T, \hat{\psi}^{B_i} \right)_{\hat{\Omega}_f} + \left(\hat{J}\frac{\mu_i}{\nu_i}(\hat{B}_i - \hat{I}), \hat{\psi}^{B_i} \right)_{\hat{\Omega}_f} \right)$$

in direction $\delta\hat{U}$ it holds:

$$\hat{A}_R^{\text{visco}\prime}(\hat{U})(\delta\hat{U}, \hat{\psi})$$

$$= \sum_{i=1}^{2} \left(\hat{J}\text{tr}(\hat{F}^{-1}\hat{\nabla}\delta\hat{u}_f)\hat{\nabla}\hat{B}_i(\hat{F}^{-1}\hat{v}_f) + \hat{J}\hat{\nabla}\delta\hat{B}_i(\hat{F}^{-1}\hat{v}_f) \right.$$

$$\left. + \hat{J}\hat{\nabla}\hat{B}_i((-\hat{F}^{-1}\hat{\nabla}\delta\hat{u}_f\hat{F}^{-1})\hat{v}_f) + \hat{J}\hat{\nabla}\hat{B}_i(\hat{F}^{-1}\delta\hat{v}_f), \hat{\psi}^{B_i} \right)_{\hat{\Omega}_f}$$

$$- \sum_{i=1}^{2} \left(\hat{J}\text{tr}(\hat{F}^{-1}\hat{\nabla}\delta\hat{u}_f)\hat{\nabla}\hat{v}_f\hat{F}^{-1}\hat{B}_i + \hat{J}\hat{\nabla}\delta\hat{v}_f\hat{F}^{-1}\hat{B}_i \right.$$

$$\left. + \hat{J}\hat{\nabla}\hat{v}_f(-\hat{F}^{-1}\hat{\nabla}\delta\hat{u}_f\hat{F}^{-1})\hat{B}_i + \hat{J}\hat{\nabla}\hat{v}_f\hat{F}^{-1}\delta\hat{B}_i, \hat{\psi}^{B_i} \right)_{\hat{\Omega}_f}$$

$$- \sum_{i=1}^{2} \left(\hat{J}\text{tr}(\hat{F}^{-1}\hat{\nabla}\delta\hat{u}_f)\hat{B}_i\hat{F}^{-T}\hat{\nabla}\hat{v}_f^T + \hat{J}\delta\hat{B}_i\hat{F}^{-T}\hat{\nabla}\hat{v}_f^T \right.$$

$$\left. + \hat{J}\hat{B}_i(-\hat{F}^{-T}\hat{\nabla}\delta\hat{u}_f^T\hat{F}^{-T})\hat{\nabla}\hat{v}_f^T + \hat{J}\hat{B}_i\hat{F}^{-T}\hat{\nabla}\delta\hat{v}_f^T, \hat{\psi}^{B_i} \right)_{\hat{\Omega}_f}$$

$$+ \sum_{i=1}^{2} \left(\frac{\mu_i}{\nu_i} \left(\hat{J}\text{tr}(\hat{F}^{-1}\hat{\nabla}\delta\hat{u}_f)(\hat{B}_i - \hat{I}) + \hat{J}\delta\hat{B}_i \right), \hat{\psi}^{B_i} \right)_{\hat{\Omega}_f}.$$

Proof Follows from calculations. □

Following the same approach we linearise the first Piola–Kirchhoff stress tensor for the Neo-Hookean material (3):

Proposition 4 *For the directional derivative of*

$$\hat{\Pi} = \mu_s\hat{J}^{-2/3}\left(\hat{F} - \frac{1}{3}\text{tr}(\hat{C})\hat{F}^{-T} \right) + \kappa_s\ln\hat{J}\hat{F}^{-T}$$

it holds

$$\partial_{\hat{u}}\hat{\Pi}(\delta\hat{u}_s)$$

$$= -\frac{2}{3}\mu_s\hat{J}^{-2/3}\text{tr}(\hat{F}^{-1}\hat{\nabla}\delta\hat{u}_s)\hat{F} + \mu_s\hat{J}^{-2/3}\hat{\nabla}\delta\hat{u}_s$$

$$+ \frac{2}{9}\mu_s\hat{J}^{-2/3}\text{tr}(\hat{F}^{-1}\hat{\nabla}\delta\hat{u}_s)\text{tr}(\hat{C})\hat{F}^{-T}$$

$$- \frac{1}{3}\mu_s\hat{J}^{-2/3}\text{tr}(\hat{\nabla}\delta\hat{u}_s^T\hat{F} + \hat{F}^T\hat{\nabla}\delta\hat{u}_s)\hat{F}^{-T}$$

$$- \frac{1}{3}\mu_s\hat{J}^{-2/3}\text{tr}(\hat{C})(-\hat{F}^{-T}\hat{\nabla}\delta\hat{u}_s^T\hat{F}^{-T})$$

$$+ \kappa_s\text{tr}(\hat{F}^{-1}\hat{\nabla}\delta\hat{u}_s)\hat{F}^{-T} + \kappa_s\ln\hat{J}(-\hat{F}^{-T}\hat{\nabla}\delta\hat{u}_s^T\hat{F}^{-T}).$$

Proof Follows from calculations. □

The remaining terms can be linearized analogously. For the sake of overview we omit the presentation of the linearization of the remaining terms.

4 Adaptivity

In this section we apply the DWR method to the viscoelastic Burgers model and to viscoelastic FSI. In Sect. 5 we use the derived error estimator for adaptive mesh refinement. A detailed presentation of the DWR method for non-linear problems can be found in [19] and [33]. One of the key steps for the error estimation is the dual solution Z which is the solution of the dual problem

$$A'(U)(\varphi, Z) = J'(U)(\varphi) \quad \forall \varphi \in V.$$

Here J denotes a goal functional like the drag or the lift. The dual problem has to be solved using higher order finite elements or employing a local higher order interpolation. For simplicity we omit possible force terms in the following derivation. The basis for the error estimation is the following result from [19].

Proposition 5 ([19]) *We have the error representation*

$$J(U) - J(U_h) = \frac{1}{2}\rho(U_h)(Z - \psi_h) + \frac{1}{2}\rho^*(U_h, Z_h)(U - \varphi_h) + \mathcal{R}_h^{(3)}$$

for all $\{\varphi_h, \psi_h\} \in V_h \times V_h$ *and the primal and dual residuals*

$$\rho(U_h)(\cdot) := -A(U_h)(\cdot),$$
$$\rho^*(U_h, Z_h)(\cdot) := J'(U_h)(\cdot) - A'(U_h)(\cdot, Z_h).$$

The remainder $\mathcal{R}_h^{(3)}$ *is cubic in the primal and dual errors.*

Proof For a proof we refer to [19]. $\qquad\square$

4.1 Stationary viscoelastic fluid

Following the approach taken in [19] we obtain the following error representation for the stationary Burgers model.

Proposition 6 *For the stationary Burgers equations it holds the following error representation*

$$J(U) - J(U_h)$$
$$\approx \sum_{K \in T_h} \Bigg(\left(-\rho_f(v \cdot \nabla)v + \nabla \cdot \mathbb{T}, z^v - \psi_h^v \right)_K$$
$$- \frac{1}{2}\left([\mathbb{T}n], z^v - \psi_h^v \right)_{\partial K \setminus \partial \Omega} + \left(\text{div} v, z^p - \psi_h^p \right)_K$$
$$- \sum_{i=1}^{2} \left(\nabla B_i v - \nabla v B_i - B_i \nabla v^T + \frac{\mu_i}{\nu_i}(B_i - I), z^{B_i} - \psi_h^{B_i} \right)_K \Bigg).$$

Here we only considered the primal residual in the error estimation to reduce the numerical costs. With this we obtain the following computable error estimator.

Proposition 7 *For the stationary Burgers equations it holds the following error approximation*

$$|J(U) - J(U_h)| \approx \sum_{K \in T_h} \eta_K, \quad \eta_K := \sum_{i=1}^{5} \rho_K^{(i)} \omega_K^{(i)}$$

with the following residuals and weights

$$\rho_K^{(1)} := \left\| -\rho_f(v \cdot \nabla)v + \nabla \cdot \mathbb{T} \right\|_K, \quad \omega_K^{(1)} := \left\| z^v - \psi_h^v \right\|_K,$$

$$\rho_K^{(2)} := \|\text{div} v\|_K, \quad \omega_K^{(2)} := \left\| z^p - \psi_h^p \right\|_K,$$

$$\rho_K^{(3)} := \frac{1}{2}h_K^{-\frac{1}{2}} \|[\mathbb{T}n]\|_{\partial K \setminus \partial \Omega}, \quad \omega_K^{(3)} := h_K^{\frac{1}{2}} \left\| z^v - \psi_h^v \right\|_{\partial K \setminus \partial \Omega},$$

$$\rho_K^{(4)} := \left\| \nabla B_1 v - \nabla v B_1 - B_1 \nabla v^T + \frac{\mu_1}{\nu_1}(B_1 - I) \right\|_K,$$

$$\omega_K^{(4)} := \left\| z^{B_1} - \psi_h^{B_1} \right\|_K,$$

$$\rho_K^{(5)} := \left\| \nabla B_2 v - \nabla v B_2 - B_2 \nabla v^T + \frac{\mu_2}{\nu_2}(B_2 - I) \right\|_K,$$

$$\omega_K^{(5)} := \left\| z^{B_2} - \psi_h^{B_2} \right\|_K.$$

4.2 Stationary viscoelastic FSI

Next we consider stationary viscoelastic FSI. We follow the approach taken in [21] for Newtonian FSI and assume $\hat{J} \approx 1$ and $\hat{F} \approx \hat{I}$. This is feasible since we only consider small deformations in the stationary benchmark in Sect. 5. With this the term involving the Cauchy stress tensor

$$\Big(\hat{J}(-\hat{p}_f \hat{I} + \hat{\rho}_f \nu_f (\hat{\nabla} v_f \hat{F}^{-1} + \hat{F}^{-T} \hat{\nabla} \hat{v}_f^T) + \mu_1(\hat{B}_1 - \hat{I})$$
$$+ \mu_2(\hat{B}_2 - \hat{I}))\hat{F}^{-T}, \hat{\nabla}\hat{\psi}_f^v \Big)$$

simplifies to

$$\left(-\hat{p}_f \hat{I} + \hat{\rho}_f \nu_f (\hat{\nabla}v_f + \hat{\nabla}\hat{v}_f^T) + \mu_1(\hat{B}_1 - \hat{I})\right.$$
$$\left. + \mu_2(\hat{B}_2 - \hat{I}), \hat{\nabla}\hat{\psi}_f^v\right).$$

In a similar way the Piola–Kirchhoff stress tensor for the STVK material is approximated by $\hat{\Pi}_{\mathrm{approx}} = \mu_s(\hat{\nabla}\hat{u}_s + \hat{\nabla}\hat{u}_s^T) + \lambda_s \widehat{\mathrm{div}}(\hat{u}_s)\hat{I}$.

Following the same approach as before we obtain the following error representation.

Proposition 8 *For the stationary viscoelastic FSI problem we obtain the following error representation*

$$J(\hat{U}) - J(\hat{U}_h)$$

$$\approx \sum_{\hat{K}_f \in \hat{T}_h} \left(\left(-\hat{\rho}_f \hat{J}(\hat{F}^{-1}\hat{v}_f \cdot \hat{\nabla})\hat{v}_f + \hat{\nabla} \cdot \hat{\mathbb{T}}_{\mathrm{appr}}, \hat{z}_f^v - \hat{\psi}_h^v\right)_{\hat{K}_f} \right.$$

$$- \frac{1}{2}\left([\hat{J}\hat{\mathbb{T}}_f \hat{F}^{-T}\hat{n}_f], \hat{z}_f^v - \hat{\psi}_h^v\right)_{\partial \hat{K}_f \backslash (\partial\hat{\Omega} \cup \hat{\Gamma}_i)}$$

$$- \left(\hat{J}\sum_{i=1}^{2}\left(\hat{\nabla}\hat{B}_i(\hat{F}^{-1}\hat{v}_f) - \hat{\nabla}\hat{v}_f\hat{F}^{-1}\hat{B}_i \right.\right.$$

$$\left.\left. - \hat{B}_i\hat{F}^{-T}\hat{\nabla}\hat{v}_f^T + \frac{\mu_i}{\nu_i}(\hat{B}_i - \hat{I}), \hat{z}_f^{B_i} - \hat{\psi}_h^{B_i}\right)\right)_{\hat{K}_f}$$

$$+ \left(\widehat{\mathrm{div}}(\hat{J}\hat{F}^{-1}\hat{v}_f), \hat{z}_f^p - \hat{\psi}_h^p\right)_{\hat{K}_f} + \left(\hat{\nabla} \cdot (\alpha_u \hat{\nabla}\hat{u}_f), \hat{z}_f^u - \hat{\psi}_h^u\right)_{\hat{K}_f}$$

$$\left.- \frac{1}{2}\left([\alpha_u \hat{\nabla}\hat{u}_f\hat{n}_f], \hat{z}_f^u - \hat{\psi}_h^u\right)_{\partial \hat{K}_f \backslash (\partial\hat{\Omega} \cup \hat{\Gamma}_i)}\right)$$

$$+ \sum_{\hat{K}_s \in \hat{T}_h} \left(\left(\hat{\nabla} \cdot \hat{\Pi}_{\mathrm{appr}}, \hat{z}_s^v - \hat{\psi}_h^v\right)_{\hat{K}_s} \right.$$

$$\left.- \frac{1}{2}\left([\hat{F}\hat{\Pi}_{\mathrm{appr}}\hat{n}_s], \hat{z}_s^v - \hat{\psi}_h^v\right)_{\partial \hat{K}_s \backslash (\partial\hat{\Omega} \cup \hat{\Gamma}_i)}\right)$$

$$- \sum_{\hat{K} \in \hat{T}_h} \left(\frac{1}{2}\left([\hat{J}\hat{\mathbb{T}}_f \hat{F}^{-T}\hat{n}_f], \hat{z}_f^v - \hat{\psi}_h^v\right)_{\hat{\Gamma}_i} \right.$$

$$\left.+ \frac{1}{2}\left([\alpha_u \hat{\nabla}\hat{u}_f\hat{n}_f], \hat{z}_f^u - \hat{\psi}_h^u\right)_{\hat{\Gamma}_i} + \frac{1}{2}\left([\hat{F}\hat{\Pi}_{\mathrm{appr}}\hat{n}_s], \hat{z}_s^v - \hat{\psi}_h^v\right)_{\hat{\Gamma}_i}\right)$$

with

$$\hat{\mathbb{T}}_{\mathrm{appr}} = -\hat{p}_f \hat{I} + \hat{\rho}_f \nu_f \left(\hat{\nabla}\hat{v}_f + \hat{\nabla}\hat{v}_f^T\right) + \mu_1(\hat{B}_1 - \hat{I}) + \mu_2(\hat{B}_2 - \hat{I}).$$

This yields the following computable error estimator.

Proposition 9 *For the stationary viscoelastic FSI problem we obtain the following error representation*

$$|J(\hat{U}) - J(\hat{U}_h)| \approx \sum_{\hat{K} \in \hat{T}_h} \eta_{\hat{K}}, \quad \eta_{\hat{K}} := \sum_{i=1}^{9} \rho_K^{(i)} \omega_K^{(i)}$$

with the following residuals and weights

$$\rho_K^{(1)} := \| -\hat{\rho}_f \hat{J}(\hat{F}^{-1}\hat{v}_f \cdot \hat{\nabla})\hat{v}_f + \hat{\nabla} \cdot \hat{\mathbb{T}}_{\mathrm{appr}}\|_{\hat{K}},$$

$$\omega_K^{(1)} := \|\hat{z}_f^v - \hat{\psi}_h^v\|_{\hat{K}},$$

$$\rho_K^{(2)} := \|\hat{\nabla} \cdot \hat{\Pi}_{\mathrm{appr}}\|_{\hat{K}},$$

$$\omega_K^{(2)} := \|\hat{z}_s^v - \hat{\psi}_h^v\|_{\hat{K}},$$

$$\rho_K^{(3)} := \|\hat{J}\left(\hat{\nabla}\hat{B}_1(\hat{F}^{-1}\hat{v}_f) - \hat{\nabla}\hat{v}_f\hat{F}^{-1}\hat{B}_1 \right.$$

$$\left. - \hat{B}_1\hat{F}^{-T}\hat{\nabla}\hat{v}_f^T + \frac{\mu_1}{\nu_1}(\hat{B}_1 - \hat{I})\right)\|_{\hat{K}},$$

$$\omega_K^{(3)} := \|\hat{z}_f^{B_1} - \hat{\psi}_h^{B_1}\|_{\hat{K}},$$

$$\rho_K^{(4)} := \|\hat{J}\left(\hat{\nabla}\hat{B}_2(\hat{F}^{-1}\hat{v}_f) - \hat{\nabla}\hat{v}_f\hat{F}^{-1}\hat{B}_2 \right.$$

$$\left. - \hat{B}_2\hat{F}^{-T}\hat{\nabla}\hat{v}_f^T + \frac{\mu_2}{\nu_2}(\hat{B}_2 - \hat{I})\right)\|_{\hat{K}},$$

$$\omega_K^{(4)} := \|\hat{z}_f^{B_2} - \hat{\psi}_h^{B_2}\|_{\hat{K}},$$

$$\rho_K^{(5)} := \|\hat{\nabla} \cdot (\alpha_u \hat{\nabla}\hat{u}_f)\|_{\hat{K}},$$

$$\omega_K^{(5)} := \|\hat{z}_f^u - \hat{\psi}_h^u\|_{\hat{K}},$$

$$\rho_K^{(6)} := \|\widehat{\mathrm{div}}(\hat{J}\hat{F}^{-1}\hat{v}_f)\|_{\hat{K}},$$

$$\omega_K^{(6)} := \|\hat{z}_f^p - \hat{\psi}_h^p\|_{\hat{K}},$$

$$\rho_K^{(7)} := \frac{1}{2}\hat{h}_K^{-\frac{1}{2}}\|[\hat{J}\hat{\mathbb{T}}_f\hat{F}^{-T}\hat{n}_f]\|_{(\partial\hat{K} \cup \hat{\Gamma}_i) \backslash \partial\hat{\Omega}},$$

$$\omega_K^{(7)} := \hat{h}_K^{\frac{1}{2}}\|\hat{z}_f^v - \hat{\psi}_h^v\|_{(\partial\hat{K} \cup \hat{\Gamma}_i) \backslash \partial\hat{\Omega}},$$

$$\rho_K^{(8)} := \frac{1}{2}\hat{h}_K^{-\frac{1}{2}}\|[\hat{F}\hat{\Pi}_{\mathrm{appr}}\hat{n}_s]\|_{(\partial\hat{K} \cup \hat{\Gamma}_i) \backslash \partial\hat{\Omega}},$$

$$\omega_K^{(8)} := \hat{h}_K^{\frac{1}{2}}\|\hat{z}_s^v - \hat{\psi}_h^v\|_{(\partial\hat{K} \cup \hat{\Gamma}_i) \backslash \partial\hat{\Omega}},$$

$$\rho_K^{(9)} := \frac{1}{2}\hat{h}_K^{-\frac{1}{2}}\|[\alpha_u \hat{\nabla}\hat{u}_f\hat{n}_f]\|_{(\partial\hat{K} \cup \hat{\Gamma}_i) \backslash \partial\hat{\Omega}},$$

$$\omega_K^{(9)} := \hat{h}_K^{\frac{1}{2}}\|\hat{z}_f^u - \hat{\psi}_h^u\|_{(\partial\hat{K} \cup \hat{\Gamma}_i) \backslash \partial\hat{\Omega}}.$$

5 Numerical results

In this section we present the numerical results. First we consider a stationary viscoelastic fluid problem. Then we analyse the convergence for global and adaptive mesh refinement for a stationary viscoelastic FSI benchmark. Next we consider the instationary FSI3 benchmark and compare our results for the Newtonian case with results from the literature. Furthermore we present the convergence results for similar time-dependent viscoelastic FSI benchmarks. Finally we apply the numerical methods to ophthalmology.

The numerical simulations are realized in the finite element library deal.ii [34]. The Newtonian FSI implementation is based on [35].

5.1 Stationary pure viscoelasticity

We start with an analysis of a stationary Oldroyd-B benchmark from the literature in order to validate the implementation of the viscoelastic fluid models and to study the convergence of the drag and the lift for global and adaptive mesh refinement. We consider pure viscoelastic fluids at first since there are no reference values available in the literature for the FSI benchmarks using viscoelastic fluids.

The domain consists of a channel with a circular obstacle (see Fig. 2). As boundary conditions we prescribe a parabolic inflow at the left boundary Γ_{in}

$$v(0,y) = \left(1.5\bar{v} \frac{y(0.41-y)}{\left(\frac{0.41}{2} \right)^2}, 0 \right),$$

the no slip condition on the top and bottom boundary Γ_{wall} and the do-nothing condition on the right boundary Γ_{out}.

Due to the inflow boundary condition for the velocity we have to adapt the boundary condition for the viscoelastic tensor B accordingly [36] to

$$B_{xx} = 1 + 2\left(\frac{v_0}{\mu_0} \frac{\partial v_x}{\partial y} \right)^2, \quad B_{xy} = \frac{v_0}{\mu_0} \frac{\partial v_x}{\partial y}, \quad B_{yy} = 1.$$

The goal functionals are the drag and the lift

$$J_{drag} = c \int_S \mathbb{T} n \cdot e_1 \, ds, \quad J_{lift} = c \int_S \mathbb{T} n \cdot e_2 \, ds$$

with $c = \frac{2}{\rho_f l_c \bar{v}^2} = 500$ where l_c is the characteristic length, $\bar{v}$ the average velocity and e_1, e_2 the unit vectors in the horizontal and vertical directions, respectively. The parameters are chosen as $v_f = 0.0005$, $\rho_f = 1.0$, $\bar{v} = 0.2$, $\mu_0 = 0.5$ and $v_0 = 0.0005$. This setup corresponds to a Reynolds number
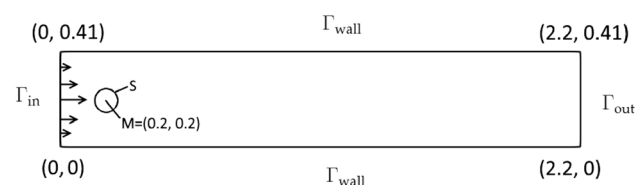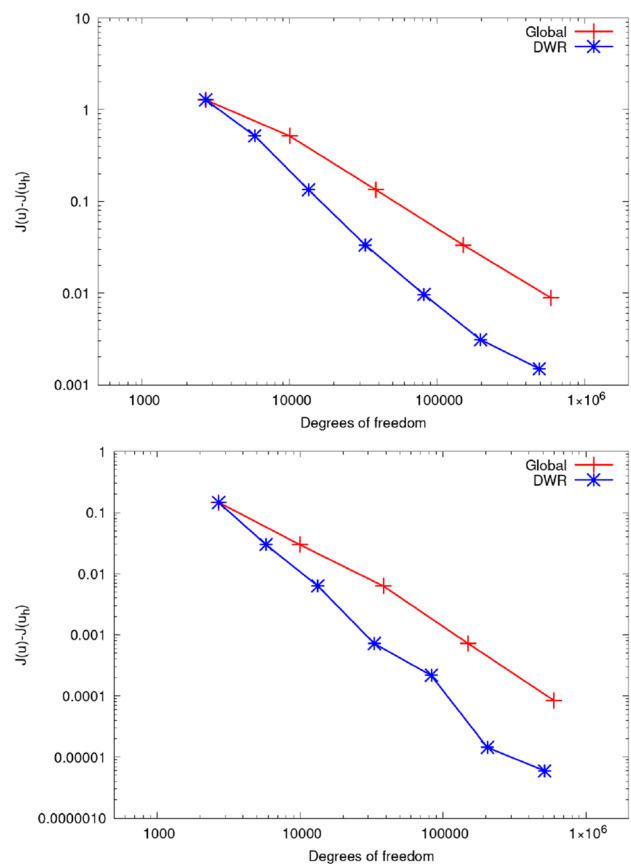

Fig. 3 Error of the drag (top) and the lift (bottom) for the Oldroyd-B benchmark

$Re = \frac{\bar{v}l_c}{v_f} = 40$ and a Weissenberg number $We = \frac{v_0}{\mu_0} \frac{\bar{v}}{l_c} = 0.002$.

Fig. 3 shows the error in the goal functionals for the drag and the lift, respectively using global refinement and adaptive refinement using the DWR method. The reference values

$$J_{drag} = 5.58351, \quad J_{lift} = 0.01052$$

are from [16]. We obtain the expected quadratic convergence. The convergence for adaptive mesh refinement is faster than for global refinement.

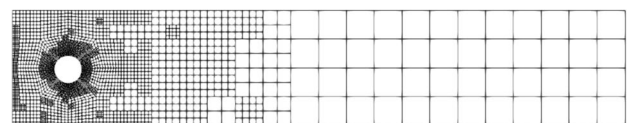Figure 4 shows the mesh after four steps of adaptive mesh refinement for the drag functional. As expected

Fig. 2 Sketch of the domain and boundaries for the flow benchmark

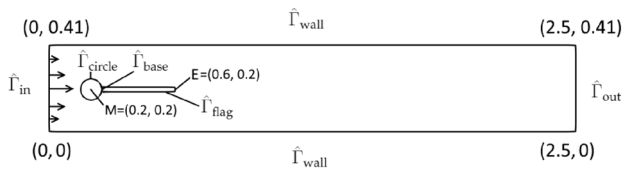**Fig. 4** The mesh after four steps of adaptive refinement for the drag functional

Fig. 5 Sketch of the domain and boundaries for the FSI benchmarks

most of the refinement is done around the circular obstacle.

5.2 Stationary viscoelastic FSI

Next we consider the stationary FSI1 benchmark introduced in [7] using the Burgers model instead of the Navier–Stokes equations. Figure 5 shows a sketch of the domain. The domain consists of a fluid channel with a circular obstacle and an elastic structure attached to the obstacle.

As boundary conditions we prescribe a parabolic inflow at the left boundary $\hat{\Gamma}_{in}$

$$v(0,y) = \left(1.5\bar{v}\frac{y(0.41-y)}{\left(\frac{0.41}{2}\right)^2}, 0\right)$$

with $\bar{v} = 0.2$. Similar to the previous benchmark we adjust the boundary conditions for the viscoelastic tensors on the inflow boundary. On the top and bottom boundary $\hat{\Gamma}_{wall}$ we prescribe the no-slip condition and on the outflow boundary $\hat{\Gamma}_{out}$ we prescribe the do-nothing condition.

The material parameters are chosen as

$$\rho_s = \rho_f = 1000, \quad v_f = 10^{-3}, \quad \mu_s = 0.5 \times 10^6,$$
$$\lambda_s = 2 \times 10^6, \quad \mu_1 = \mu_2 = 25, \quad v_1 = v_2 = 0.125.$$

This setup for the Burgers model corresponds to the Oldroyd-B model with $\mu_0 = 50$ and $v_0 = 0.25$.

The drag and lift coefficients are defined as

$$J_{drag} := \int_{\hat{S}} (\hat{J}\hat{\mathbb{T}}_f \hat{F}^{-T})\hat{n}_f \cdot e_1 \, d\hat{s},$$

$$J_{lift} := \int_{\hat{S}} (\hat{J}\hat{\mathbb{T}}_f \hat{F}^{-T})\hat{n}_f \cdot e_2 \, d\hat{s}$$

with $\hat{S} := \hat{\Gamma}_{flag} \cup (\hat{\Gamma}_{circle} \setminus \hat{\Gamma}_{base})$. Here $\hat{\Gamma}_{flag}$ denotes the part of the beam which has a common interface to the fluid domain and $\hat{\Gamma}_{base}$ is the remainder of the beam which is part of the circular obstacle (see Fig. 5).

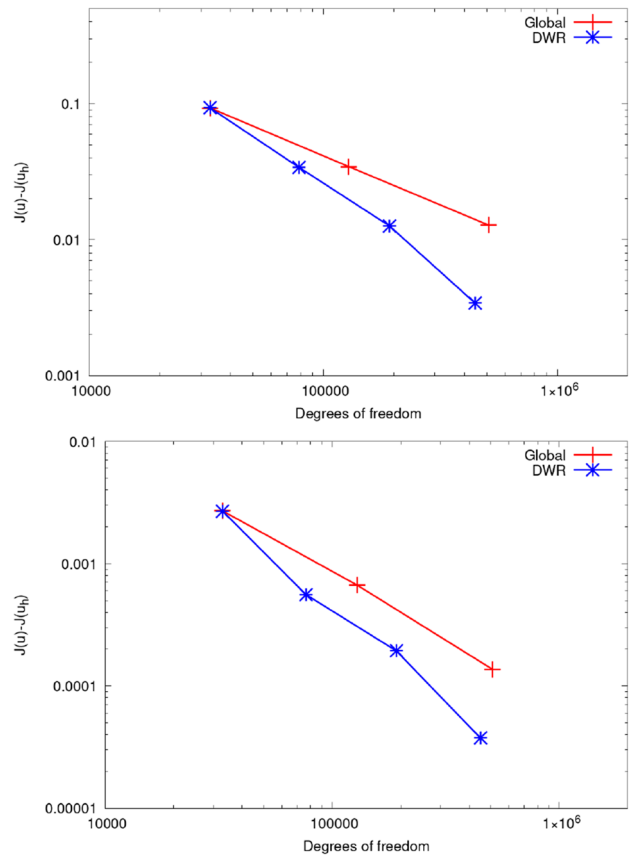Figure 6 shows a comparison between global refinement and adaptive mesh refinement using the DWR method for

Fig. 6 Error of the drag (top) and the lift (bottom) for the viscoelastic FSI1 benchmark

the drag and the lift. Similar to the pure fluid case the convergence using the adaptive mesh refinement strategy is faster than for global refinement. Due to the lack of knowledge of the exact reference value the convergence in the last step of the adaptive refinement might be overestimated. In addition we do not obtain the optimal convergence order because of the limited regularity of the solution due to the reentrant corner of the beam as in the Newtonian FSI case [22].

5.3 Time-dependent FSI

Next we analyse instationary benchmark problems with large deformations and a higher Reynolds number.

5.3.1 Time-dependent Newtonian FSI

We start with a comparison of the results for the Newtonian FSI3 benchmark introduced in [7]. The setup is similar to the previous benchmark with the following inflow on $\hat{\Gamma}_{in}$

Table 1 Results for the quantities of interest for the mean and the amplitude on three different mesh levels with 19248, 75712 and 300288 degrees of freedom with two different time step sizes Δt for the Newtonian FSI3 benchmark

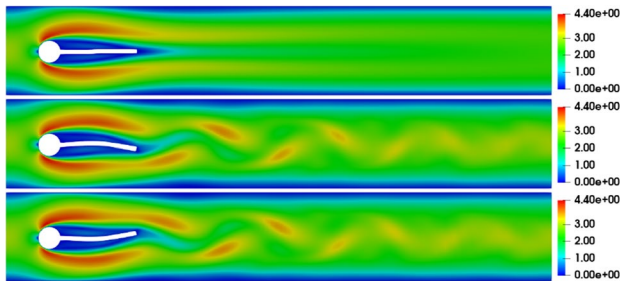| Dofs	Δt	$u_x(A) \times 10^{-3}$	$u_y(A) \times 10^{-3}$	Drag	Lift
19248	0.001	-2.82 ± 2.67	1.50 ± 34.24	451.56 ± 22.75	2.11 ± 157.39
75712	0.001	-2.80 ± 2.64	1.47 ± 34.37	457.49 ± 25.35	2.23 ± 155.89
300288	0.001	-2.85 ± 2.69	1.47 ± 34.76	459.57 ± 26.86	2.14 ± 158.90
19248	0.0005	-2.83 ± 2.67	1.50 ± 34.24	451.45 ± 22.66	2.14 ± 156.75
75712	0.0005	-2.80 ± 2.64	1.47 ± 34.36	457.38 ± 25.28	2.32 ± 155.07
300288	0.0005	-2.85 ± 2.69	1.46 ± 34.75	459.47 ± 26.80	2.23 ± 157.98
ref. [37]		-2.88 ± 2.72	1.47 ± 34.99	460.5 ± 27.74	2.50 ± 153.9

Fig. 7 Velocity magnitude in Ω_f at three different times for the viscoelastic FSI3 case

$$v(0, y) = \left(1.5\bar{v} \frac{y(0.41 - y)}{\left(\frac{0.41}{2} \right)^2}, 0 \right)$$

with a smooth increase in the beginning

$$v(t, 0, y) = \begin{cases} v(0, y) \frac{1 - \cos(\frac{\pi}{2} t)}{2} & \text{if } t < 2.0 \\ v(0, y) & \text{else.} \end{cases}$$

The parameters are given by

$$\rho_f = \rho_s = 10^3, \quad v_f = 10^{-3}, \quad \mu_s = 2 \cdot 10^6, \quad \lambda_s = 8 \times 10^6$$

and $\bar{v} = 2.0$. This yields a Reynolds number $\mathrm{Re} = 200$. The quantities of interest are the displacement at the point $E = (0.6, 0.2)$, the drag and the lift. Since this setup results

in a periodic time-dependent solution we consider the mean and the amplitude of the functionals.

Table 1 shows the results for three different mesh sizes and two different time step sizes. The results are in very good agreement with the available literature [7, 37].

5.3.2 Time-dependent viscoelastic FSI

Next we analyse the FSI3 benchmark using the Burgers model. For the first case we choose the parameters as in the Newtonian FSI3 benchmark with the additional parameters chosen as $\mu_1 = \mu_2 = 50$ and $\nu_1 = \nu_2 = 0.25$. Figure 7 shows the velocity magnitude in the current fluid domain Ω_f at three different times.

Table 2 shows the results for the functionals for three mesh sizes and two different time step sizes. The table shows stable results in all functionals and convergence in time and in space. Furthermore the table shows that the viscoelasticity of the fluid has a significant influence on the four quantities of interest in comparison to the Newtonian FSI case for the chosen parameters.

Since the FSI3 benchmark is a numerically challenging problem due to the large displacements and the fast movement of the beam we consider a potentially easier setup where we choose a stiffer elastic material with $\mu_s = 3.5 \times 10^6$, $\lambda_s = 1.4 \times 10^7$. This results in a smaller amplitude of the x- and y-displacement at the point E. Table 3 shows the results for global mesh refinement and shows that in this setup the results for the functionals yield an acceptable accuracy even on a relatively coarse

Table 2 Results for the quantities of interest for the mean and the amplitude on four different mesh levels with 11044, 42336, 165664 and 655296 degrees of freedom with two different time step sizes Δt for the viscoelastic FSI3 benchmark

Dofs	Δt	$u_x(A) \times 10^{-3}$	$u_y(A) \times 10^{-3}$	Drag	Lift
11,044	0.001	-1.78 ± 1.73	1.21 ± 27.52	513.14 ± 15.45	6.76 ± 154.57
42,336	0.001	-1.13 ± 1.07	1.57 ± 21.31	509.86 ± 10.33	0.42 ± 115.75
165,664	0.001	-1.25 ± 1.18	1.53 ± 22.53	513.63 ± 12.29	0.69 ± 119.61
655,296	0.001	-1.25 ± 1.18	1.53 ± 22.53	513.95 ± 12.57	0.82 ± 119.47
11,044	0.0005	-1.79 ± 1.73	1.20 ± 27.53	513.29 ± 15.38	6.80 ± 154.05
42,336	0.0005	-1.13 ± 1.07	1.57 ± 21.28	509.65 ± 10.25	0.44 ± 115.46
165,664	0.0005	-1.24 ± 1.18	1.53 ± 22.48	513.29 ± 12.19	0.75 ± 119.14
655,296	0.0005	-1.25 ± 1.18	1.53 ± 22.54	513.92 ± 12.52	0.82 ± 119.34

Table 3 Results for the quantities of interest for the mean and the amplitude on four different mesh levels with 11044, 42336, 165664 and 655296 degrees of freedom for the viscoelastic FSI3 benchmark with $\mu_s = 3.5 \times 10^6$ and $\lambda_s = 1.4 \times 10^7$

Dofs	Δt	$u_x(A) \times 10^{-3}$	$u_y(A) \times 10^{-3}$	Drag	Lift
11044	0.001	-1.01 ± 1.01	1.23 ± 19.10	504.21 ± 14.51	6.75 ± 288.04
42336	0.001	-0.51 ± 0.48	1.65 ± 12.99	503.11 ± 7.71	1.75 ± 185.37
165664	0.001	-0.71 ± 0.69	1.58 ± 15.77	506.99 ± 11.62	2.10 ± 218.59
655296	0.001	-0.72 ± 0.70	1.57 ± 15.97	507.62 ± 12.13	2.17 ± 220.93
11044	0.0005	-1.01 ± 1.01	1.23 ± 19.12	504.21 ± 14.49	6.77 ± 288.18
42336	0.0005	-0.51 ± 0.48	1.65 ± 13.00	503.11 ± 7.70	1.76 ± 185.44
165664	0.0005	-0.71 ± 0.69	1.58 ± 15.79	507.00 ± 11.62	2.12 ± 218.61
655296	0.0005	-0.72 ± 0.70	1.57 ± 15.98	507.63 ± 12.13	2.19 ± 220.94

Fig. 8 Plots of the functionals for the Newtonian FSI3 case and two viscoelastic cases with varying shear moduli μ_1 and μ_2
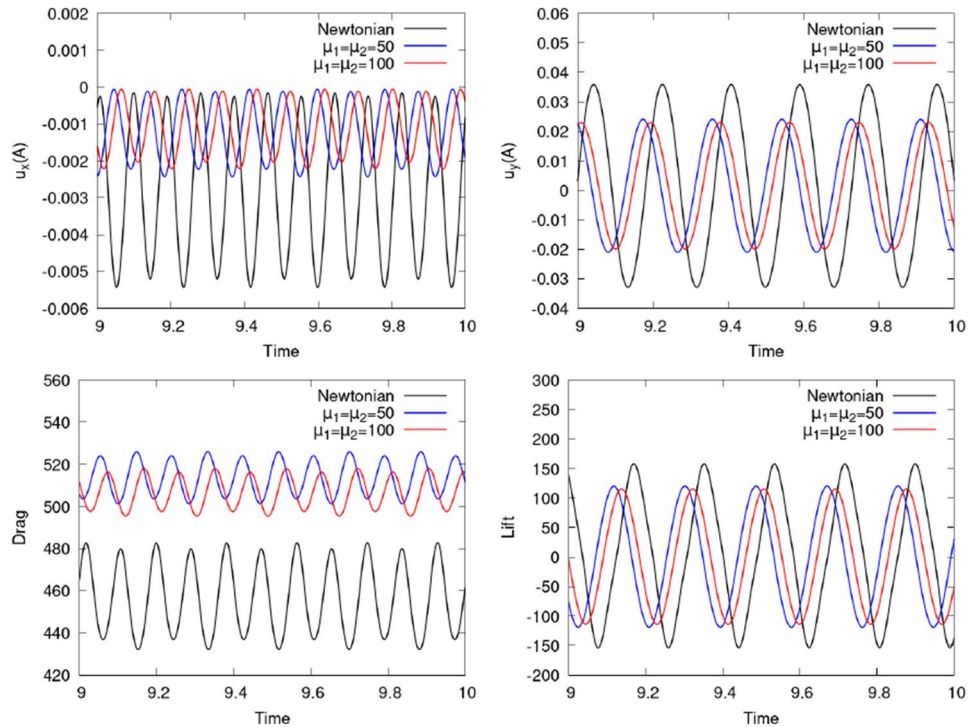

mesh. The exception to this is the lift functional which still changes substantially after two global refinement steps.

Next we analyse the effect of different parameters for the viscosity and shear moduli on the movement of the beam and the forces acting on it. Figure 8 shows a comparison of the plots for the Newtonian FSI3 case and two viscoelastic cases. The first one is the previously studied case with $\mu_1 = \mu_2 = 50$ and $\nu_1 = \nu_2 = 0.25$. In the second case we increase the shear moduli to $\mu_1 = \mu_2 = 100$. The plots show that in the viscoelastic cases the amplitude of the displacement, the drag and the lift decreases in comparison to the Newtonian case since the viscoelasticity slows down the movement of the beam. In particular the maximal y-displacement decreases from 0.036 in the Newtonian case to 0.024 in the first viscoelastic case. Similarly the minimal y-displacement increases from

−0.033 to −0.021. The minimum of the x-displacement increases from −0.0055 to −0.0024. We obtain very similar results for the displacement and the lift for the two viscoelastic cases. The drag values differ slightly more between the two viscoelastic cases and are much higher than the drag for the Newtonian FSI case. This is mainly due to the forces acting on the circular obstacle and not due to the forces on the interface.

Next we analyse different values for the viscosities ν_1 and ν_2. Figure 9 shows a comparison of the functionals for different sets of parameters. The first two cases are the Newtonian FSI case and the viscoelastic case with $\nu_1 = \nu_2 = 0.25$ which were already discussed. For the other viscoelastic cases we choose $\nu_1 = \nu_2 = 0.05$ and $\nu_1 = \nu_2 = 0.005$, respectively. The plots show that for decreasing viscosities ν_1 and ν_2 the mean and the

Fig. 9 Plots of the functionals for the Newtonian FSI3 case and three viscoelastic cases with with varying viscosities v_1 and v_2
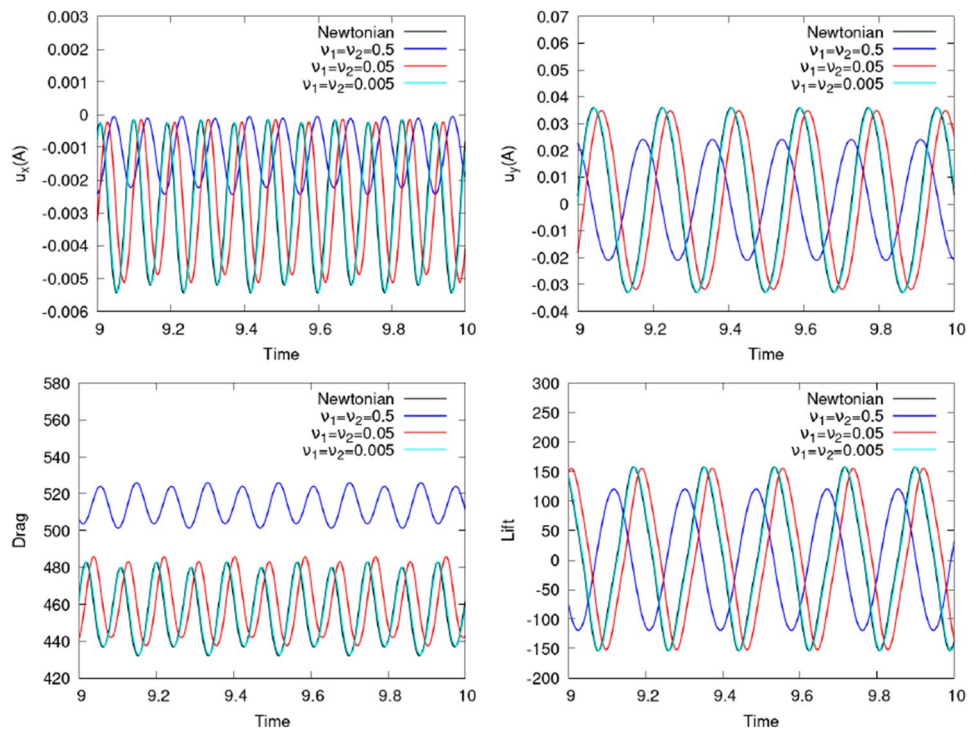
amplitude of the functionals approach the values of the Newtonian case.

These results show that the viscoelasticity of the fluid can have a big influence on the displacement, the drag and the lift in comparison to the Newtonian case.

5.4 Applications in ophthalmology

Finally we consider an application in ophthalmology. In experiments in [8] bovine eyes were analysed during stretch experiments. For the experiments the eyes were cut horizontally at the top and the bottom. The eyes were then fixed on the left side of the eye and pulled to the right on the right side.

Our goal is to perform similar simulations on a human eye geometry to analyse the difference between a healthy and a non-healthy eye. The healthy vitreous is viscoelastic and thus modelled using the Burgers equations following [6]. In the non-healthy case the vitreous is modelled by the Newtonian Navier–Stokes equations. This pathology is motivated by vitrectomies which are medical procedures during which the vitreous is replaced by a fluid-like substance. Therefore a comparison between the healthy viscoelastic and the liquefied vitreous is of interest. Table 4 shows the chosen parameters which have been previously collected in [24].

Figure 10 shows the 3D mesh used for the numerical simulations. Similar to the experiments the eye was

Table 4 Material parameters of the elastic structures (top) and parameters for the fluid domain (bottom) for human eyes

Parameter	Units	Value	Computation	Source
μ_s (sclera)	Pa	330×10^3	330×10^3	[27]
μ_s (lens)	Pa	$0.19 - 59.6 \times 10^3$	10×10^3	[38]
κ_s (sclera)	Pa	–	330×10^6	[27]
κ_s (lens)	Pa	–	10×10^6	[27]
$\hat{\rho}_s$ (sclera)	kg/m^3	1.076×10^3	1.05×10^3	[39]
$\hat{\rho}_s$ (lens)	kg/m^3	1.104×10^3	1.05×10^3	[39]
$\hat{\rho}_f$	kg/m^3	$1.0053 - 1.0089 \times 10^3$	1.007×10^3	[40]
μ_1	Pa	1.07×10^{-1}	1.07×10^{-1}	[6]
v_1	Pa s	9200.28	9200.28	[6]
μ_2	Pa	6.99×10^{-2}	6.99×10^{-2}	[6]
v_2	Pa s	4.17	4.17	[6]
v_f (healthy)	Pa s	8.53×10^{-4}	8.53×10^{-4}	[6]
v_f (liquefied)	Pa s	7.322×10^{-7}	7.322×10^{-7}	[41]

cut horizontally in the middle. The colors indicate the fluid (blue) and the structure domains (grey and darkgrey). The fluid domain corresponds to the vitreous and the darkgrey and grey parts correspond to the lens and the sclera, respectively. On the left we fix the eye in x-direction $u_x = 0$. On the right boundary we prescribe a displacement $u_x = g$. The remaining components and boundaries are left free to move.
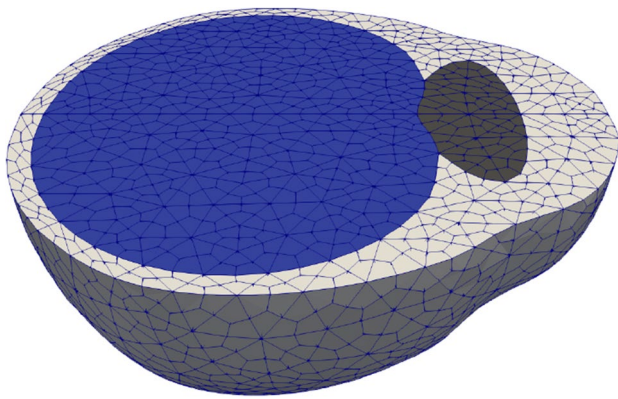
Fig. 10 Mesh with 11,568 cells and 1,175,422 degrees of freedom [304,053 (velocity), 304,053 (displacement), 20,704 (pressure), 546,612 (viscoelastic tensors)]
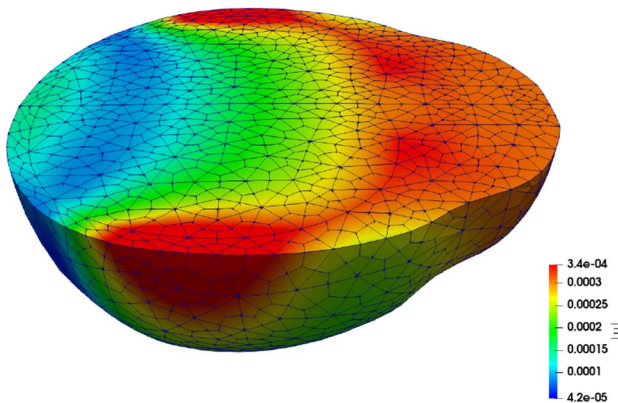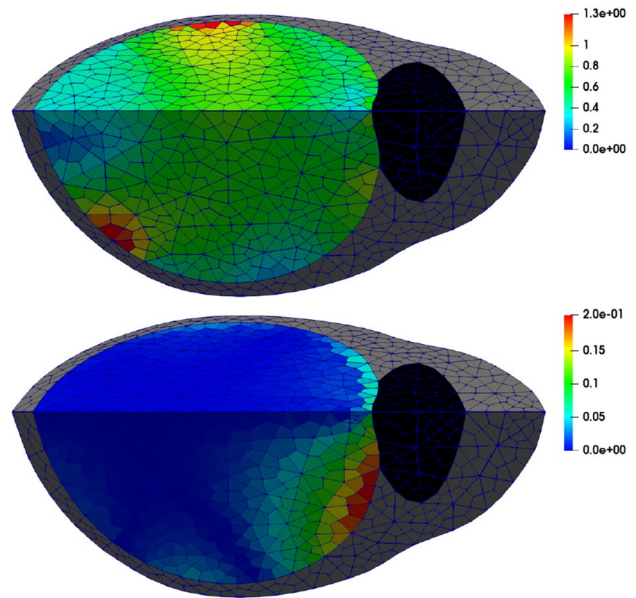

Fig. 11 Displacement magnitude after 0.1 s

Fig. 12 Average norm per cell of the transformed Cauchy stress tensor $\hat{J}\hat{\mathbb{T}}_f\hat{F}^{-T}$ in the vitreous for the Burgers (top) and the Navier–Stokes (bottom) case. The domain is cut vertically for visualization purposes

Figure 11 shows the displacement magnitude after 0.1 s. Figure 12 shows a comparison of the average norm per cell of the transformed Cauchy stress tensor in the vitreous for a healthy vitreous and a liquefied vitreous. The maximum stress in the healthy eye is higher by a factor of 6.5. This is an interesting result since some medical diseases in the eye are possibly linked to the stress distribution in the vitreous.

6 Conclusion

In this work we derived a numerical solution method for viscoelastic FSI in the ALE framework. We derived a monolithic variational formulation which was discretized in time, using the shifted Crank–Nicolson scheme and then in space using the finite element method. Furthermore we calculated the necessary directional derivatives for Newton's method. We applied the DWR method to viscoelastic fluids and viscoelastic FSI. The numerical results showed the superiority of the DWR method in comparison to global refinement for a pure viscoelastic and a viscoelastic FSI benchmark. Next we showed the convergence of goal functionals like the drag, the lift and the displacement at a point for time-dependent viscoelastic FSI in time and in space. Furthermore we analysed different sets of parameters and their influence on the goal functionals. The results showed that the viscoelastic properties of the fluid can have a big impact on the displacement of the beam, the drag and the lift.

Finally we applied the numerical solution methods to ophthalmology. The simulations showed big differences between the stress in the healthy and the liquefied vitreous, with the stress in the healthy vitreous being 6.5 times higher than in the liquefied vitreous.

Data avaiibility The datasets generated during the current study are available in Kobra (Kassel online library, repository and archive), kobra.uni-kassel.de.

Declarations

Conflict of interest The authors have no relevant financial or non-financial interests to disclose.

Ethical approval This article does not contain any studies with human participants or animals performed by any of the authors.

References

1. Quarteroni A, Veneziani A, Zunino P (2001) Mathematical and numerical modeling of solute dynamics in blood flow and arterial walls. SIAM J Numer Anal 39(5):1488–1511
2. Razzaq M, Turek S, Hron J, Acker J, Weichert F, Grunwald I, Roth C, Wagner M, Romeike B (2010) Numerical simulation and benchmarking of fluid-structure interaction with application to hemodynamics. In: Fundamental trends in fluid–structure interaction. World Scientific, Singapore, pp 171–199
3. Hsu MC, Bazilevs Y (2012) Fluid–structure interaction modeling of wind turbines: simulating the full machine. Comput Mech 50(6):821–833
4. Johnston BM, Johnston PR, Corney S, Kilpatrick D (2004) Non-newtonian blood flow in human right coronary arteries: steady state simulations. J Biomech 37(5):709–720
5. Sharif-Kashani P, Hubschman JP, Sassoon D, Kavehpour HP (2011) Rheology of the vitreous gel: Effects of macromolecule organization on the viscoelastic properties. J Biomech 44(3):419–423
6. Tram NK, Swindle-Reilly KE (2018) Rheological properties and age-related changes of the human vitreous humor. Front Bioeng Biotechnol 6:199
7. Turek S, Hron J (2006) Proposal for numerical benchmarking of fluid–structure interaction between an elastic object and laminar incompressible flow. In: Bungartz H-J, Schäfer M (eds) Fluid–structure interaction: modelling, simulation, and optimisation. Springer, Berlin, pp 371–385
8. Shah NS, Beebe DC, Lake SP, Filas BA (2016) On the spatiotemporal material anisotropy of the vitreous body in tension and compression. Ann Biomed Eng 44(10):3084–3095
9. Donea J, Giuliani S, Halleux JP (1982) An arbitrary Lagrangian–Eulerian finite element method for transient dynamic fluid–structure interactions. Comput Methods Appl Mech Eng 33(1–3):689–723
10. Amestoy PR, Duff IS, L'Excellent JY (2000) Multifrontal parallel distributed symmetric and unsymmetric solvers. Comput Methods Appl Mech Eng 184(2–4):501–520
11. Formaggia L, Quarteroni A, Veneziani A (2009) Cardiovascular mathematics: modeling and simulation of the circulatory system, vol 1. Springer, Milan
12. Richter T, Wick T (2010) Finite elements for fluid–structure interaction in ale and fully eulerian coordinates. Comput Methods Appl Mech Eng 199(41–44):2633–2642
13. Schäfer M, Heck M, Yigit S (2006) An implicit partitioned method for the numerical simulation of fluid–structure interaction. In: Bungartz H-J, Schäfer M (eds) Fluid–structure interaction: modelling. simulation, optimisation. Springer, Berlin, pp 171–194
14. Nobile F, Vergara C (2012) Partitioned algorithms for fluid–structure interaction problems in haemodynamics. Milan J Math 80(2):443–467
15. Dunne T (2006) An eulerian approach to fluid–structure interaction and goal-oriented mesh adaptation. Int J Numer Methods Fluids 51(9–10):1017–1039
16. Damanik H, Hron J, Ouazzi A, Turek S (2012) Monolithic Newton-multigrid solution techniques for incompressible nonlinear flow models. Int J Numer Methods Fluids 71(2):208–222
17. Tůma K (2013) Identification of rate type fluids suitable for modeling geomaterials. PhD thesis, Charles University in Prague
18. Hron J, Rajagopal K, Tůma K (2014) Flow of a burgers fluid due to time varying loads on deforming boundaries. J Non-Newton Fluid Mech 210:66–77
19. Becker R, Rannacher R (2001) An optimal control approach to a posteriori error estimation in finite element methods. Acta Numer 10(1):1–102
20. Braack M, Richter T (2006) Solutions of 3D Navier–Stokes benchmark problems with adaptive finite elements. Comput Fluids 35(4):372–392
21. Wick T (2012) Goal-oriented mesh adaptivity for fluid–structure interaction with application to heart-valve settings. Arch Mech Eng 59(1):73–99
22. Richter T (2012) Goal-oriented error estimation for fluid–structure interaction problems. Comput Methods Appl Mech Eng 223:28–42
23. Wang W, Qian X, Song H, Zhang M, Liu Z (2016) Fluid and structure coupling analysis of the interaction between aqueous humor and iris. BioMed Eng OnLine 15(2):569–586
24. Tůma K, Stein J, Průša V, Friedmann E (2018) Motion of the vitreous humour in a deforming eye–fluid–structure interaction between a nonlinear elastic solid and viscoleastic fluid. Appl Math Comput 335:50–64
25. Burgers J (1939) Mechanical considerations—model systems—phenomenological theories of relaxation and of viscosity. First report on viscosity and plasticity. Nordemann Publishing, New York, pp 5–67
26. Simo JC, Taylor RL, Pister KS (1985) Variational and projection methods for the volume constraint in finite deformation elasto-plasticity. Comput Methods Appl Mech Eng 51(1–3):177–208
27. Grytz R, Fazio MA, Girard MJ, Libertiaux V, Bruno L, Gardiner S, Girkin CA, Downs JC (2014) Material properties of the posterior human sclera. J Mech Behav Biomed Mater 29:602–617
28. Heywood JG, Rannacher R, Turek S (1996) Artificial boundaries and flux and pressure conditions for the incompressible Navier–Stokes equations. Int J Numer Methods Fluids 22(5):325–352

29. Wick T (2011) Adaptive finite element simulation of fluid–structure interaction with application to heart-valve dynamics. PhD thesis, University of Heidelberg

30. Richter T (2017) Fluid–structure interactions: models, analysis and finite elements, vol 118. Lecture notes in computational science and engineering. Springer, Cham

31. Heywood JG, Rannacher R (1990) Finite-element approximation of the nonstationary Navier–Stokes problem. Part IV: error analysis for second-order time discretization. SIAM J Numer Anal 27(2):353–384

32. Holzapfel GA (2000) Nonlinear solid mechanics: a continuum approach for engineering. Wiley, Chichester

33. Bangerth W, Rannacher R (2003) Adaptive finite element methods for differential equations. Birkhäuser, Boston

34. Arndt D, Bangerth W, Davydov D, Heister T, Heltai L, Kronbichler M, Maier M, Pelteret JP, Turcksin B, Wells D (2021) The deal.II finite element library: design, features, and insights. Comput Math Appl 81:407–422

35. Wick T (2013) Solving monolithic fluid–structure interaction problems in arbitrary Lagrangian Eulerian coordinates with the deal.II library. Arch Numer Softw 1(1):1–19

36. Dou HS, Phan-Thien N (1999) The flow of an oldroyd-b fluid past a cylinder in a channel: adaptive viscosity vorticity (DAVSS-ω) formulation. J Non-Newton Fluid Mech 87(1):47–73

37. Turek S, Hron J, Razzaq M, Wobker H, Schäfer M (2010) Numerical benchmarking of fluid–structure interaction: a comparison of different discretization and solution approaches. In: Bungartz H-J, Mehl M, Schäfer M (eds) Fluid structure interaction II: modelling. simulation, optimization, Springer, Berlin, pp 413–424

38. Wilde GS, Burd HJ, Judge SJ (2012) Shear modulus data for the human lens determined from a spinning lens test. Exp Eye Res 97(1):36–48

39. Su X, Vesco C, Fleming J, Choh V (2009) Density of ocular components of the bovine eye. Optometry Vis Sci 86(10):1187–1195

40. Murphy W, Black J, Hastings G (eds) (2016) Handbook of biomaterial properties. Springer, New York

41. Vennard JK (2011) Elementary fluid mechanics. Read Books Ltd, Redditch

Publisher's Note Springer Nature remains neutral with regard to jurisdictional claims in published maps and institutional affiliations.